SUBMITTED TO THE ASTROPHYSICAL JOURNAL
Preprint typeset using LaTeX style emulateapj v. 8/13/10

PSR J2022+3842: AN ENERGETIC RADIO AND X-RAY PULSAR ASSOCIATED WITH SNR G76.9+1.0

Z. ARZOUMANIAN[1,2], E. V. GOTTHELF[3], S. M. RANSOM[4], S. SAFI-HARB[5], R. KOTHES[6], AND T. L. LANDECKER[6]

Submitted to The Astrophysical Journal

ABSTRACT

We present *Chandra X-ray Observatory*, Robert C. Byrd Green Bank Radio Telescope (GBT), and *Rossi X-ray Timing Explorer* (*RXTE*) observations directed toward the radio supernova remnant (SNR) G76.9+1.0. The *Chandra* investigation reveals a hard, unresolved X-ray source coincident with the midpoint of the double-lobed radio morphology and surrounded by faint, compact X-ray nebulosity. These features suggest that an energetic neutron star is powering a pulsar wind nebula (PWN) seen in synchrotron emission. Indeed, the spatial relationship of the X-ray and radio emissions is remarkably similar to the extended emission around the Vela pulsar. A follow-up pulsation search with the GBT uncovered a highly-dispersed (DM $= 427 \pm 1$ pc cm^{-3}) and highly-scattered pulsar with a period of 24 ms. Its subsequently measured spin-down rate implies a characteristic age $\tau_c = 8.9$ kyr, making PSR J2022+3842 the most rapidly rotating young radio pulsar known. With a spin-down luminosity $\dot{E} = 1.2 \times 10^{38}$ erg s^{-1}, it is the second-most energetic Galactic pulsar known, after the Crab pulsar. The 24-ms pulsations have also been detected in the *RXTE* observation; the combined *Chandra* and *RXTE* spectral fit suggests that the *Chandra* point-source emission is virtually 100% pulsed. The 2–16 keV spectrum of the narrow (0.06 cycles FWHM) pulse is well-fitted by an absorbed power-law model with column density $N_{\rm H} = (1.7 \pm 0.5) \times 10^{22}$ cm^{-2} and photon index $\Gamma = 1.0 \pm 0.2$, strongly suggestive of magnetospheric emission. For an assumed distance of 10 kpc, the 2–10 keV luminosity of $L_{\rm X} = 6.9 \times 10^{33}$ erg s^{-1} suggests one of the lowest known X-ray conversion efficiencies $L_{\rm X}/\dot{E} = 5.8 \times 10^{-5}$, similar to that of the Vela pulsar. Finally, the PWN around PSR J2022+3842 revealed by *Chandra* is also underluminous, with $F_{\rm PWN}/F_{\rm PSR} \lesssim 1$ in the 2–10 keV band, a further surprise given the pulsar's high spin-down luminosity.

Subject headings: pulsars: individual (CXOU J202221.68+384214.8, PSR J2022+3842) — stars: neutron — supernova remnants — X-rays: stars

1. INTRODUCTION

The past decade has been witness to a highly productive back-and-forth relationship between X-ray and radio observations of rotation-powered pulsars. Nonthermal Galactic radio sources that serve as tracers of particle acceleration have motivated follow-up X-ray imaging, most notably with the Chandra telescope. The X-ray data for supernova remnants (SNRs) have, in many instances, revealed the presence of point-like sources surrounded by nebulae, typically axisymmetric, consistent with outflows of relativistic particle winds from a central engine (e.g., the powerful time-varying magnetic fields in a pulsar magnetosphere). Finally, targetted radio periodicity searches of these objects have uncovered previously unseen pulsations, providing the spin periods and, eventually, estimated ages, magnetic field strengths, and spin-down luminosities without which a meaningful physical understanding of the surrounding phenomena would be beyond reach. A few specific examples of this general picture of radio/X-ray symbiosis have been the discoveries of the pulsars in the remnants 3C58, G54.1+0.3, G292.0+1.8, and in the "Mouse" (see, e.g., Camilo 2004).

SNR G76.9+1.0 was discovered in a 480 MHz DRAO survey of the Cygnus X region and initially characterized as an extragalactic object (Wendker et al. 1991). Follow-up three-band radio observations using the Very Large Array (VLA) by Landecker et al. (1993) resolved a two-lobed structure $4'$ in size, with a connecting bridge of emission, embedded in a faint, roughly circular emitting region $9' \times 12'$ across. Based on its steep, non-thermal spectrum, polarization, and extended morphology, similar to center-filled SNRs, these authors favored a SNR interpretation. In this picture, the radio lobes trace the Crab-like synchrotron emission of a pulsar wind nebula. Landecker et al. (1993) resolved a weak radio source near the center of the bridge in the 4.86 GHz VLA image, but further qualified this signal as a likely noise fluctuation.

In this letter, we present imaging, spectral, and timing studies of X-ray and radio observations of G76.9+1.0 culminating in the discovery of PSR J2022+3842, the pulsations of which are visible in both bands, and its associated X-ray PWN. In §??, we present analysis of the *Chandra* data on the pulsar and its surrounding faint diffuse emission. In §??, we describe the discovery and follow-up radio timing observations of PSR J2022+3842, together with the pulse properties and a long-term timing ephemeris. In §??, we present the results of a deep

Zaven.Arzoumanian@nasa.gov
[1] Center for Research and Exploration in Space Science and Technology and X-ray Astrophysics Laboratory, NASA Goddard Space Flight Center, Code 662, Greenbelt, MD 20771, USA
[2] Universities Space Research Association, Columbia, MD 21044, USA
[3] Columbia Astrophysics Laboratory, Columbia University, 550 West 120th Street, New York, NY 10027, USA
[4] National Radio Astronomy Observatory, 520 Edgemont Road, Charlottesville, VA 22901, USA
[5] Canada Research Chair. Department of Physics and Astronomy, University of Manitoba, Winnipeg, MB, R3T 2N2, Canada
[6] National Research Council of Canada, Herzberg Institute of Astrophysics, Dominion Radio Astrophysical Observatory, Box 248, Penticton, BC, V2A 6J9, Canada

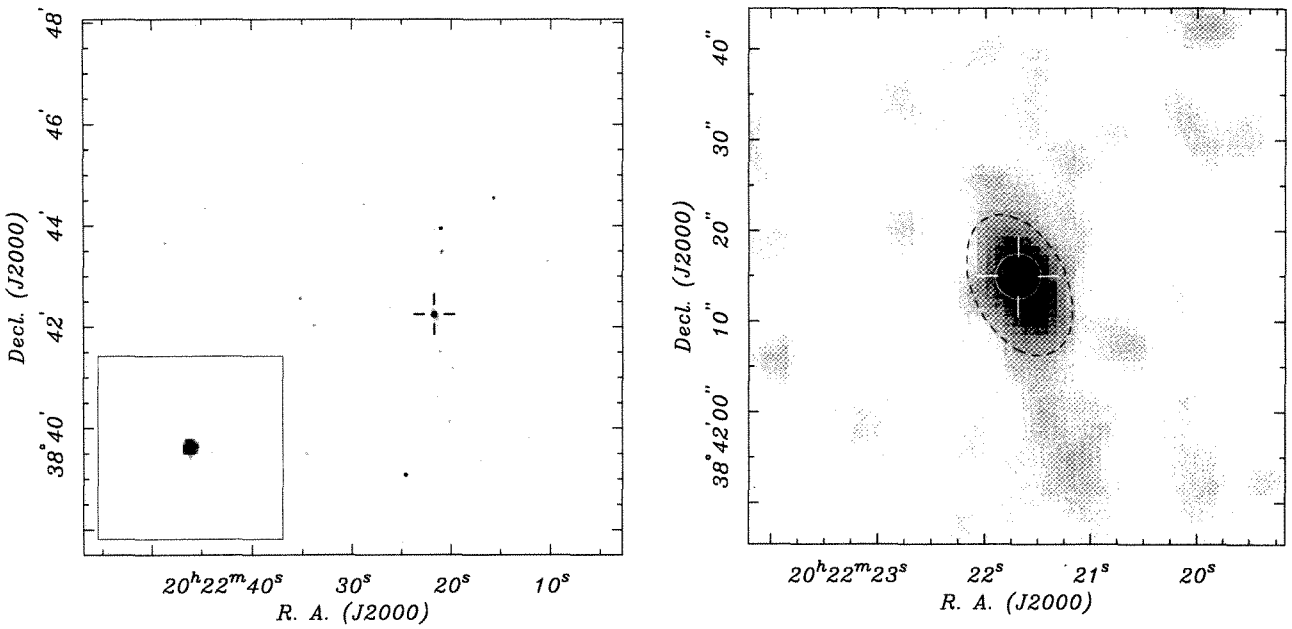

Figure 1. *Chandra* ACIS-S3 1.5–10 keV X-ray image of the center of G76.9+1.0. *Left*: The smoothed, exposure corrected image is scaled to emphasize the field point sources. The cross indicates CXOU J202221. The *inset* shows the raw, unsmoothed pixel image around this source. *Right*: Expanded image around CXOU J202221, which has been excised to highlight the surrounding diffuse emission (see text). The location and size of the source extraction region is indicated by the white circle.

RXTE observation. We show that the pulsed emission is consistent with the *Chandra* source cementing its association with the SNR. For reasons outlined below, we adopt a distance to G76.9+1.0 of 10 kpc throughout this work.

2. *CHANDRA* OBSERVATIONS AND RESULTS

SNR G76.9+1.0 was observed for 54 ks by the *Chandra* observatory on 2005 August 01 UT using the Advanced CCD Imaging Spectrometer (ACIS; Burke et al. 1997) operating in the full-frame TIMED/VFAINT exposure mode (ObsID #5586). This detector is sensitive to X-rays in the 0.3–12 keV energy range with a resolution of $\Delta E/E \sim 0.06$ FWHM at 1 keV. The CCD pixel scale is 0.5″, comparable to the telescope's on-axis spatial resolution. We reduced and analyzed the data using the CIAO (V4.3), FTOOLS (V6.10), CALDB (V4.4.2), and XSPEC (V12.6.0q) X-ray analysis software packages. A total of 53.7 ks of live-time was accumulated. No additional time filtering was necessary as the background rate was stable over the course of the observation. We followed the CIAO online science threads to create ACIS spectra and images. To allow for imaging with the best available angular resolution, we disabled pixel randomization (used by default in standard CIAO data reduction to avoid spatial digitization effects); we also applied the sub-pixel event localization algorithm described by Mori et al. (2001).

Figure 1 presents the exposure-corrected image in the 1.5 – 10 keV band of the ACIS-S3 CCD covering the center of the SNR field. No morphological evidence of G76.9+1.0 itself is apparent nor is there any hint of large-scale diffuse emission in images created in the soft (< 2 keV) or hard (> 2 keV) energy bands; instead, several faint point-like sources are detected. The brightest of these, marked by the cross in Figure 1, is located close to the optical axis and contains $N = 1112$ photons. This source lies within 14″ of the discounted radio point source of Landecker et al. (1993) and is the only X-ray source within 1′; this suggests that the radio feature may be related given the 15″ radio beam size, perhaps representing a radio PWN or the pulsar itself. Further evidence for a pulsar interpretation is provided by the faint but distinct X-ray nebulosity surrounding this object. To highlight this emission, in Figure 1 (right panel) we show an expanded image around the nebula with the source pixels nulled and the resulting image smoothed with a Gaussian kernel of $\sigma = 1.5$ pixels. There is a clear excess of emission along a diagonal axis (PA = 26°); see Figure 2. This argues against a dust scattered halo, expected to be symmetric.

To refine the location of the bright source, the X-ray image was registered using the coordinates of 8 2MASS infrared counterparts obtained from the NASA/IPAC Infrared Science Archive. The updated centroid is located at (J2000.0) R.A = $20^{\rm h}22^{\rm m}21\overset{\rm s}{.}689$, Decl. = +38°42′14″.82 with a 1σ uncertainty of (0″.09, 0″.07) in the two coordinates, respectively. The required shift in R.A. and Decl. was (−0″.012, −0″.162). This source, CXOU J202221.68+384214.8, is hereafter referred to by the shortened name CXOU J202221.

We extracted a spectrum for CXOU J202221 using a nominal $r = 2\overset{''}{.}5$ aperture centered on the source and generated an appropriate response matrix using the `specextract` CIAO script. The diffuse emission and cosmic and detector backgrounds contribute negligibly ($\sim$ 10 counts) in this region. With a maximum count rate in a pixel of $< 4 \times 10^{-3}$ s^{-1}, photon pile-up can safely be ignored. The spectrum was grouped with a minimum of 50 counts per spectral channel and fitted using XSPEC to an absorbed non-thermal power-law model, a common property of young, rotation-powered pulsars. An excellent fit ($\chi^2 = 13$ for 19 DoF) was obtained for an absorbing column $N_{\rm H} = (1.4 \pm 0.5) \times 10^{22}$ cm^{-2} and

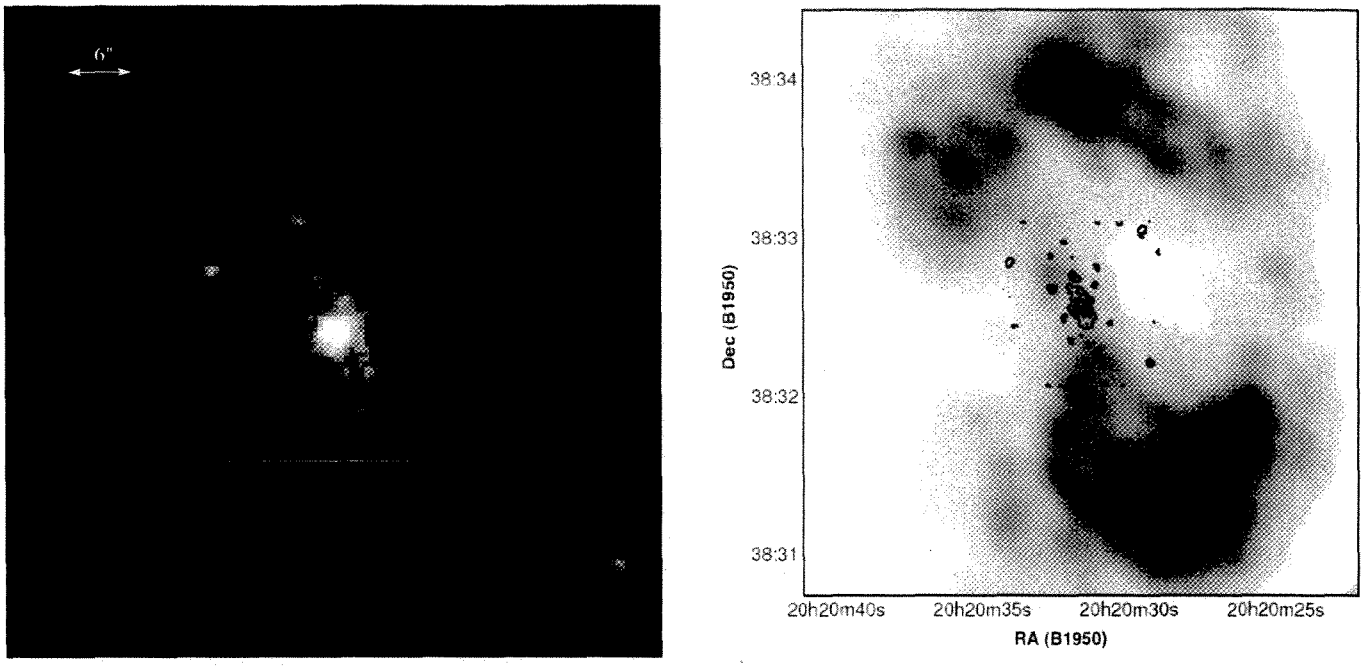

Figure 2. (*Left:*) Adaptively smoothed (see text) *Chandra* 0.5–7 keV image of the X-ray emission from the central regions of G76.9+1.0. The suggested morphology of a point source within an axisymmetric structure is reminiscent of the compact nebula surrounding the Vela pulsar. (*Right:*) Contours of the same smoothed image superposed on a 4.86 GHz image obtained with the VLA (see (Landecker et al. 1993) for details). The unambiguous alignment of the long axis of the diffuse X-ray emission with the symmetry axis of the double-lobed radio emission lends credence to the identification of the extended X-ray feature with a pulsar wind nebula. The location of the X-ray nebula in a region of depressed emission between the radio lobes is also strikingly similar to the radio/X-ray configuration around Vela; see, e.g., Figure 10 of Dodson et al. (2003).

photon index $\Gamma = 0.8 \pm 0.3$ (90% confidence intervals are used throughout). The absorbed 2–10 keV source flux is $F_{\rm PSR} = 6.1 \times 10^{-13}$ erg cm^{-2} s^{-1}, implying an isotropically beamed luminosity of $L_{\rm X} = 7.3 \times 10^{33} D_{10}$ erg s^{-1}.

The faintness of the nebula does not allow an independent spectral fit. Instead, to estimate its flux, we fixed the column density to the point source fit value and assume a nominal absorbed power-law model with $\Gamma = 1.4$, derived from the spectral index trend between energetic pulsars and their nebulae reported by Gotthelf (2004). We extracted $N = 84 \pm 13$ background-subtracted photons for the nebula from an elliptical region with radii $8\farcs3 \times 5\farcs1$ centered on the pulsar, with the source region excluded. The absorbed 2–10 keV flux for the putative PWN is $F_{\rm PWN} \approx 2 \times 10^{-13}$ erg cm^{-2} s^{-1}. The flux ratio $F_{\rm PWN}/F_{\rm PSR} \approx 0.3$ is well below that expected for similarly energetic pulsars (Gotthelf 2004).

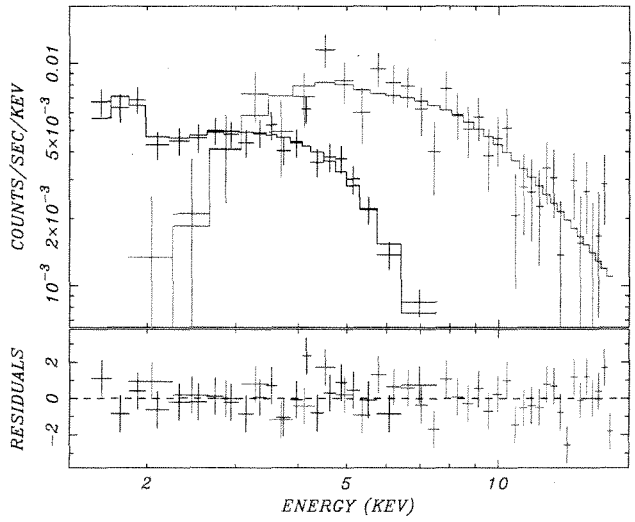

Figure 3. The *Chandra* ACIS-S3 spectrum of CXOU J202221 (*black*) and the *RXTE* PCA spectrum of the pulsed emission from PSR J2022+3842 (*red*), fitted jointly to an absorbed power-law model, with the normalizations untied. The solid line shows the best fit model (see text). The pulsed *RXTE* flux is obtained by subtracting the off-peak spectrum from the on-peak spectrum. Residuals from the best fit are shown in units of standard deviation.

3. GBT OBSERVATIONS AND RESULTS

The GBT Spectrometer SPIGOT data-acquisition backend was used for 5 hours on each of two days, with 600 MHz bandwidth centered at 1.95 GHz. The instrument provided 768 channels with 16-bit sampling of summed polarizations at 82 μs intervals. The PRESTO software Ransom et al. (2002) was used to search for pulsations, and a candidate 24-ms periodicity was detected on both days with formal significances of 7σ on MJD 54397 and 12σ on MJD 54400. Confirmation observations were carried out on 2009 May 6 (MJD 54957) using the GUPPI data-acquisition system configured similarly to the discovery instrumentation; resulting output from the search code is shown in Figure 4. A search for single "giant" pulses yielded no compelling candidates, despite the fact that the pulsar's estimated magnetic field strength at the light cylinder, suggested to be relevant in the production of giant pulses (Cognard et al. 1996), is approximately 70% that of both the Crab pulsar and PSR B1937+21, and comparable to that of PSR B1821−24, all of which exhibit giant pulses.

The pulsar's flux density at 2 GHz is approximately 75 μJy, comparable to other young, faint pulsars discov-

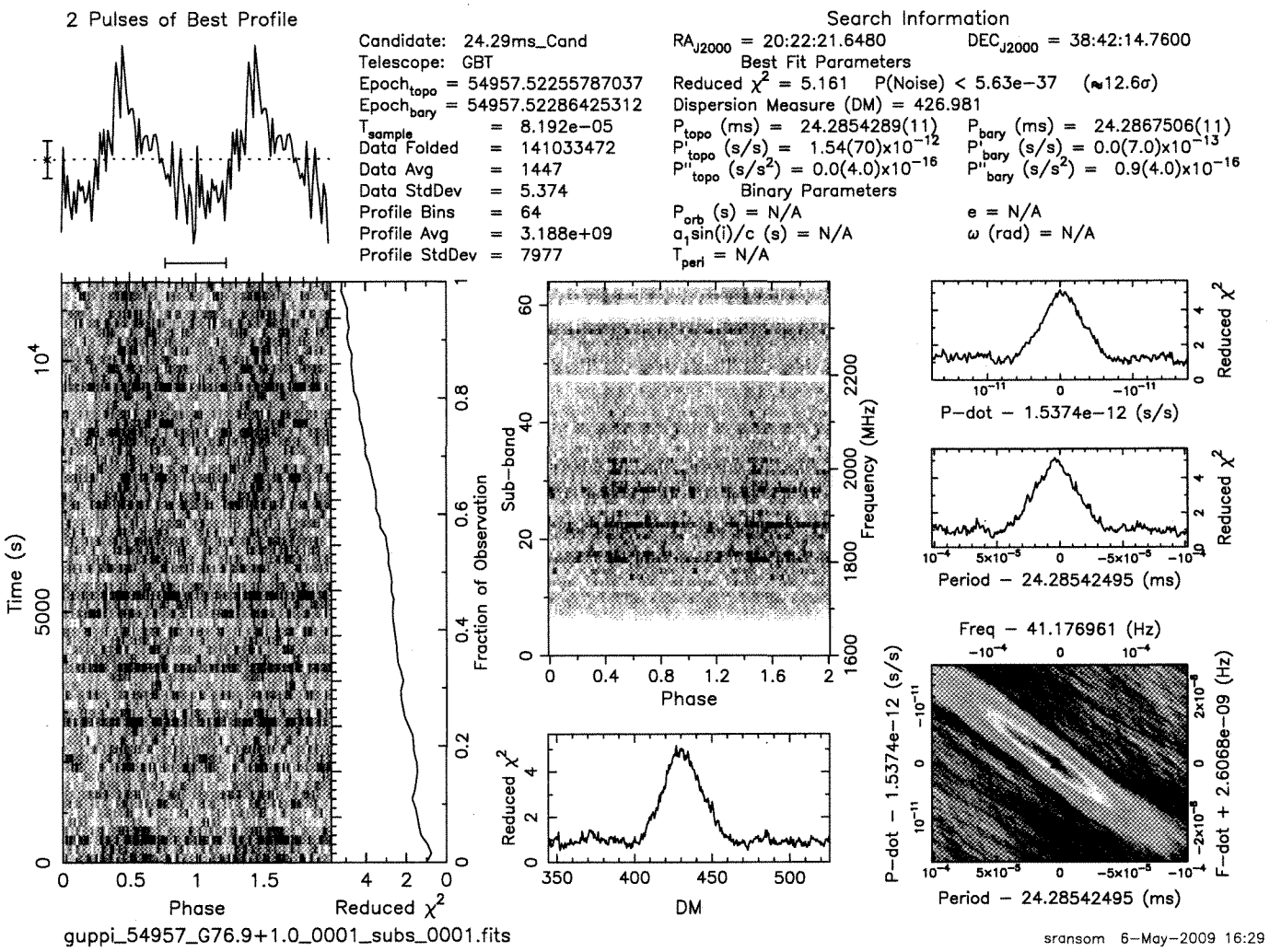

Figure 4. Discovery of radio pulsations at 1.95 GHz from PSR J2022+3842.

ered in deep searches of SNRs, and PSR J2022+3842 appears to have a steep spectrum, $\alpha \simeq 3$, similar to that of the Crab pulsar. The NE2001 Galactic electron distribution model (Cordes & Lazio 2002) fails to accommodate the dispersion measure of 427 pc cm^{-3} in the direction of PSR J2022+3842—formally, the model suggests a lower bound on the distance to the pulsar of 50 kpc. Instead, a likely over-density of free electrons in the Cygnus region, along the line of sight, accounts for the higher-than-expected dispersion. In this direction, the Perseus Arm lies at a distance of $\lesssim 7$ kpc, and the Outer Arm at $\gtrsim 10$ kpc. For convenience in scaling distance-dependent parameters and because the larger distance brings X-ray efficiencies roughly in line with those of other young pulsars, we adopt a distance $d = 10 D_{10}$ kpc.

The NE2001 model also predicts a timescale for pulse broadening due to interstellar scattering of 0.3 ms at 1 GHz; instead, we find $\tau_{1\mathrm{GHz}} = 90 \pm 20$ ms, which scales (as $\nu^{-4.4}$) to ~ 5 ms at the center of our observing band. Consistent with this result, exploratory observations centered at 800 MHz and 1.4 GHz failed to detect the pulsar; a similar attempt at 5 GHz yielded a weak detection, but of an unexpectedly broad pulse. Thus, despite the importance of scatter-broadening at the lower frequencies, the pulse appears to be intrinsically broad ($\sim 1/3$ of the pulse period). The well-established trend of pulse widths increasing as $P^{-0.5}$ underestimates this result by a factor of 2–3 (e.g., for the outermost conal component of Mitra & Deshpande 1999).

Additional radio observations, also with the GUPPI system, were carried out at roughly 3-month intervals to constrain the pulsar's long-term timing behavior (Figure 5). The long-term spin ephemeris from these observations is shown in Table 1. Notably, the pulse period measured during the confirmation observation and later differs substantially from that detected during the two discovery observations 1.5 years earlier, implying that a spin "glitch" occurred at an unknown epoch in this interval. The discrete change in period P associated with the glitch was $\Delta P/P \simeq 1.9 \times 10^{-6}$.

4. *RXTE* OBSERVATIONS AND RESULTS

The field containing CXOU J202221 was observed by *RXTE* for a total of 99 ks spanning 7 days beginning on 2010 January 27 - February 4 UT (observation P95316). The data were collected with the Proportional Counter Array (PCA; Jahoda et al. 1996) in the GoodXenon mode with an average of 1.8 out of the five proportional counter units (PCUs) active. In this mode, photons are time-tagged to 0.9 μs and have an absolute uncertainty

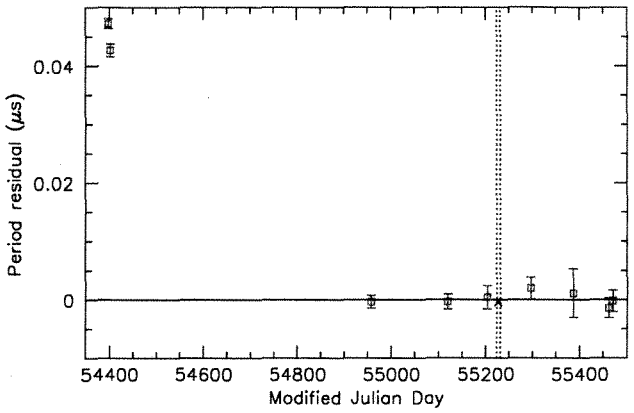

Figure 5. Pulse period evolution of PSR J2022+3842 at 2 GHz (*red squares*), and in 2–20 keV X-rays (*blue cross*, with 1σ uncertainty smaller than the plotted symbol). Residuals are relative to the timing model shown in Table 1, and the vertical dotted lines mark the start and end dates of the *RXTE* observation. The pulse period at the discovery epoch of the radio pulsations, around MJD 54400, was significantly longer than the stable value at later times, indicating that a spin-up glitch occurred at some point before the confirmation observation near MJD 55000.

better than 100 μs (Rots et al. 1998). The effective area of five combined detectors is approximately 6500 cm^2 at 10 keV with a roughly circular field-of-view of $\sim 1^\circ$ FWHM. Spectral information is available in the 2–60 keV energy band with a resolution of $\sim 16\%$ at 6 keV.

PCA production data for this observation were obtained from NASA's HEASARC archive and time filtered using the standard criteria. This rejected intervals of South Atlantic Anomaly passages, Earth occultations, and other periods of high particle activity, resulting in a total of 94.2 ks of usable data. The photon arrival times were transformed to the solar system barycenter in Barycentric Dynamical Time (TDB) using the JPL DE200 ephemeris and the *Chandra*-derived coordinates of CXOU J202221 presented in Table 1.

4.1. *Timing Analysis*

The timing analysis was restricted to PCA channels 2–50, corresponding to the $\approx$ 2–20 keV energy range, and from the top Xenon layer of each PCU, to optimize the signal-to-noise for a typical pulsar spectrum. Because of the long observation span, photon detection times were accumulated in 4 ms bins and a 2^{28}-point accelerated Fast Fourier Transform (FFT) was performed to search for a periodic signal, testing a range of plausible frequency derivatives. This immediately revealed a signal at 24 ms of sufficient strength to analyze short intervals of data and build up a fully phase-coherent timing solution using the TOA (time of arrival) method, described as follows.

The *RXTE* observations of CXOU J202221 were spread over the 7 days and clustered into 10 groups of two, three, or four adjacent 96 minute orbits, with large gaps in between. For each of these groups, we were able to extracted the period and phase of the signal with sufficiently small uncertainties to maintain cycle counts between fitted epochs. We generated pulse profiles for the peak period using the Z_n^2 test (Buccheri et al. 1983) with $n = 10$ harmonics to allow for the sharp profile.

Table 1
Timing Parameters of PSR J2022+3842

Parameter	Value
R.A. (J2000)[a]	$20^h22^m21^s.689(6)$
Decl. (J2000)[a]	$+38°42'14''.82(7)$
Epoch (MJD TDB)	55227.00000027
Period, P (ms)	24.2877561082(84)
Period derivative, $\dot{P}$	$4.3192(27) \times 10^{-14}$
Range of timing solution (MJD)	55223–55231
Characteristic age, τ_c (kyr)	8.9
Spin-down luminosity, $\dot{E}$ (erg s^{-1})	1.18×10^{38}
Surface dipole magnetic field, B_s (G)	1.03×10^{12}

Note. — 1σ uncertainties given in parentheses.
[a] *Chandra* ACIS-S3 position registered using 2MASS objects (see text).

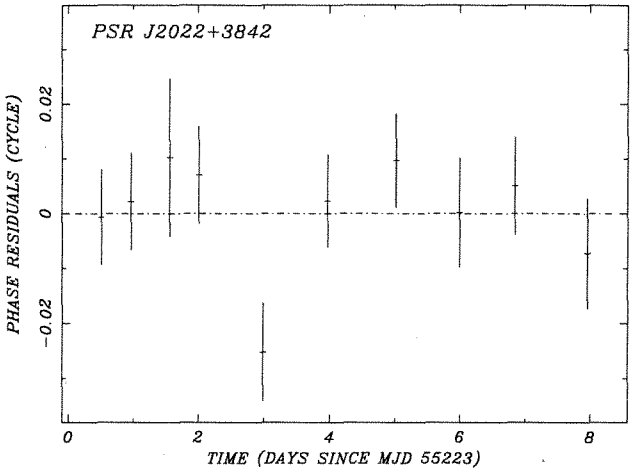

Figure 6. Phase residuals for PSR J2022+3842 after fitting the quadratic ephemeris of Table 1 to a set of *RXTE* PCA X-ray observations.

The resulting profiles were cross correlated, shifted, and summed to generate a master pulse profile template. Individual profiles were then cross-correlated with the template to determine the time of phase zero (TOA) and its uncertainty at each epoch.

The derived TOAs were iteratively fitted to a quadratic ephemeris using the TEMPO software. We started by fitting TOAs from the first three most closely spaced TOAs to a linear solution, and then iteratively added the next TOA. At each step we found that the new TOA would match to < 0.02 cycles the predicted phase derived from the previous set. The resulting ephemeris referenced to the mid-point of the observation is presented in Table 1 and the phase residuals are shown in Figure 6. The residuals are all less than 0.02 cycles and appear to be random within their statistical uncertainties, with the exception of a single 3σ data point ($\Delta\phi = 0.025 \pm 0.01$) for which an investigation finds no reason to exclude.

Figure 7 displays the pulse profile using all of the 2–20 keV data folded on the final ephemeris. It has a single symmetric peak that is triangular in shape and narrow, with a FWHM of only 0.06 of a full cycle. The measured pulsed emission is 0.91% of the total PCU data; however, as will be shown below, the intrinsic signal is nearly 100% pulsed compared to the flux derived from the spectrum of CXOU J202221. We see no energy dependence of the

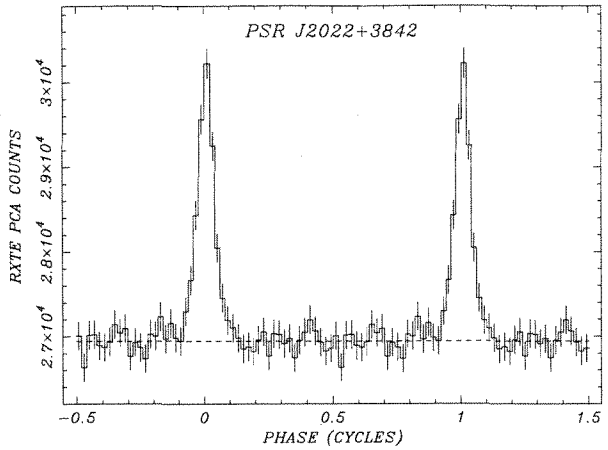

Figure 7. *RXTE* folded light curve of PSR J2022+3842 in the 2–20 keV band. Phase zero corresponds to the epoch of the ephemeris in Table 1. Two cycles are shown for clarity.

pulse profile when subdividing the 2–20 keV *RXTE* energy range.

4.2. *RXTE Spectral Analysis*

The pulsed-flux spectrum of PSR J2022+3842 can be isolated through phase-resolved spectroscopy. We used the FTOOLS `fasebin` software to construct phase-dependent spectra based on the ephemeris of Table 1. We combined spectra from all observation intervals using only data recorded in the top Xenon layer of PCU#2; this PCU was (uniquely) used for all observation intervals over the 7 days. Similarly, we averaged the standard PCA responses generated for each epoch. In fitting the pulsed flux, the unpulsed emission provides a near perfect background estimate. The spectra were accumulated in two phase intervals representing the "off-peak" and "on-peak" emission and fitted in the 2–16 keV range using XSPEC.

Based on the *Chandra* spectrum, we fitted an absorbed power-law model with the interstellar absorption held fixed at $N_{\rm H} = 1.4 \times 10^{22}$ cm^{-2}; leaving the $N_{\rm H}$ unconstrained results in a larger uncertainty in Γ. The resulting best-fit photon index is $\Gamma = 1.0 \pm 0.2$ with $\chi^2 = 29$ for 32 DoF. The absorbed 2–10 keV flux for the pulsed emission is 5.3×10^{-13} erg cm^{-2} s^{-1}, which represents, within statistics, all of the point-source flux of PSR J2022+3842 measured for CXOU J202221, indicating that its intrinsic pulsed fraction is nearly 100%. In Figure 3, we show the result of a joint fit to the pulsed emission from PSR J2022+3842 and CXOU J202221 leaving only the normalization free. The best fit parameters are $N_{\rm H} = (1.7 \pm 0.5) \times 10^{22}$ cm^{-2} and $\Gamma = 1.0 \pm 0.2$ with $\chi^2 = 49$ for 53 DoF. There is no indication of spectral curvature in the fitted energy range, as found for several other energetic pulsars (e.g., Crab and Vela). The absorbed 2–10 keV flux for CXOU J202221 and pulsed PSR J2022+3842 is 5.8×10^{-13} erg cm^{-2} s^{-1} and 5.2×10^{-13} erg cm^{-2} s^{-1}, respectively. We take these fitted parameters as the reported values.

5. DISCUSSION

There can be little doubt that CXOU J202221 and PSR J2022+3842 are one and the same, and thus the pulsar is located to arcsec precision. The non-thermal X-ray source lies at the center of G76.9+1.0, lacks an optical counterpart, and has nebular emission suggestive of a PWN. Most importantly, the pulsed flux detected using *RXTE* accounts for nearly all of the *Chandra* emission. These properties are consistent with the magnetic dipole model of a pulsar whose X-ray emission is powered by rotational energy losses.

PSR J2022+3842 is outstanding in several respects. It is the second-most energetic Galactic pulsar known, after the Crab pulsar, and the fourth overall, taking into account two LMC pulsars, in N157B ($P = 16$ ms, PSR J0537−6910) and in SNR 0540−69 ($P = 50$ ms). It is also the second-most rapidly rotating young pulsar after J0537−6910, and the shortest-period radio-bright pulsar known. In contrast, for a distance of 10 kpc, it is among the least efficient at converting its spin-down luminosity into X-rays, with an $\eta \equiv L_{2-10\,\rm keV}/\dot{E} = 5.8 \times 10^{-5}$, similar to the much less energetic Vela pulsar.

PSR J2022+3842 clearly lacks the bright X-ray PWN expected from an energetic pulsar. Most notably, PSR J2022+3842 is only the second example (of some 20) of an energetic pulsar with $\dot{E} \gtrsim 4 \times 10^{36}$ erg s^{-1} without a bright PWN relative to the pulsar emission ($F_{PWN}/F_{PSR} \gtrsim 1$), defying the trend presented in Gotthelf (2004). As such it is most similar in properties to PSR J1617−5055 (Torii et al. 1998), the 69 ms pulsar with $\dot{E} = 1.6 \times 10^{37}$ erg s^{-1}, $B_s = 3.1 \times 10^{12}$ G, and 8.1 kyr. The missing PWNe in these cases remain unexplained.

The hard spectral index of PSR J2022+3842 also sets it apart from the typical young, energetic pulsar, deviating significantly from the observed trend $\Gamma \propto 1/\sqrt{\dot{E}}$ (Gotthelf 2003, 2–10 keV), which predicts an index of $\Gamma = 1.8$. Such flat power laws are mostly found for pulsars with H.E.S.S. counterparts (e.g., PSR J1838−0655, Gotthelf & Halpern 2008).

PSR J2022+3842 is clearly a pulsar with unusual properties requiring further investigation. Multi-wavelength searches might be fruitful in providing important components for its understanding. Based on the spin-down energy and given the subarcsec coordinates and X-ray ephemeris, PSR J2022+3842 is a good candidate for a search for gamma-ray pulsations using Fermi data. However, the absence of a bright PWN makes it an unlikely TeV target, even though its spectral properties suggest otherwise.

Support for this work was provided by the National Aeronautics and Space Administration through Chandra Award Number GO5-6077Z issued by the Chandra X-ray Observatory Center, which is operated by the Smithsonian Astrophysical Observatory for and on behalf of the National Aeronautics Space Administration under contract NAS8-03060. This work made use *RXTE* data provided by the High Energy Astrophysics Archive at NASA's Goddard Space Flight Center.

REFERENCES

Arzoumanian, Z., Safi-Harb, S., Ransom, S., Kothes, R., & Landecker, T. 2010, COSPAR 38th Scientific Assembly, Bremen, Germany July 18-25, 2010
Buccheri, R., et al 1983, A&A, 128, 245

Burke, B. E., Gregory, J., Bautz, M. W., Prigozhin, G. Y., Kissel, S. E., Kosicki, B. N., Loomis, A. H., & Young, D. J. 1997, IEEE Trans. Electron Devices, 44, 1633
Cognard, I., Shrauner, J. A., Taylor, J. H., & Thorsett, S. E. 1996, ApJ, 457, L81
Cordes, J. M., & Lazio, T. J. W. 2002, arXiv:astro-ph/0207156
Dodson, R., Lewis, D., McConnell, D., & Deshpande, A. A. 2003, MNRAS, 343, 116
Gotthelf, E. V. 2003, ApJ, 591, 361
Gotthelf, E. V. 2004, in Young Neutron Stars and Their Environments, Ed. F. Camilo & B. M. Gaensler (San Fran., CA), IAU Symp. 214, 225
Gotthelf, E. V. & Halpern, J. P. 2008, ApJ, 681, 515
Jahoda, K., Swank, J. H., Giles, A. B., Stark, M. J., Strohmayer, T., Zhang, W., & Morgan, E. H. 1996, Proc. SPIE, 2808, 59
Landecker, T. L., Higgs, L. A., & Wendker, H. J 1993, A&A, 276, 522
Mitra, D., & Deshpande, A. A. 1999, A&A, 346, 906
Mori, K., Tsunemi, H., Miyata, E., Baluta, C. J., Burrows, D. N., Garmire, G. P., & Chartas, G. 2001, in ASP Conf. Ser. 251, New Century of X-ray Astronomy, ed. H. Inoue & H. Kunieda (San Francisco: ASP), 576
Ransom, S. M., Eikenberry, S. S., & Middleditch, J. 2002, AJ, 124, 1788
Rots, A. H., et al. 1998, ApJ, 501, 749
Torii, K., et al. 1998, ApJ, 494, L207
Wendker, H. J. 1991, Higgs, L. A, Landecker, T. L. 1991, A&A, 241, 551